On the potential use of two-photon polymerization to 3D print chromatographic packed bed supports

Matheuse, Fréderick; Vanmol, Koen; Van Erps, Jürgen; De Malsche, Wim; Ottevaere, Prof. Dr. Ir. Heidi; Desmet, Gert

Published in:
Journal of Chromatography. A

DOI:
10.1016/j.chroma.2021.462763

Publication date:
2021

License:
CC BY-NC-ND

Document Version:
Accepted author manuscript

On the Potential Use of Two-Photon Polymerization to 3D print Chromatographic Packed Bed Supports for Analytical Scale Chromatography

Fréderick Matheuse[1], Koen Vanmol[2], Jürgen Van Erps[2], Wim De Malsche[1], Heidi Ottevaere[2], Gert Desmet[1,*]

[1]*Department of Chemical Engineering, Vrije Universiteit Brussel, Brussels, Belgium*

[2]*Department of Applied Physics and Photonics, Vrije Universiteit Brussel and Flanders Make, Brussels, Belgium*

Abstract

The continuous quest for chromatographic supports offering kinetic performance properties superior to that of the packed bed of spheres has pushed the field to consider alternative formats such as for example monolithic and pillar array columns. This quest seems bound to culminate in the use of 3D printing technology, as this intrinsically offers the possibility to produce supports with a perfect uniformity and with a size and shape that is fully optimized for the chromatographic separation process. The present contribution investigates the use of the 3D printing technology with the highest possible resolution available today, i.e., two-photon polymerization (2PP). It is shown that 2PP printing is capable of achieving the $\leq$1 µm printing resolution needed to be competitive with that of state-of-the-art packed bed HPLC columns. Depending on the laser scan speed, the lower limit through-pore size for a tetrahedral skeleton monolith with a theoretical 80% external porosity was found to be at 800 nm, whne printing at a scan speed of 50 mm/s with a laser power of 10%. For a scan speed of 10 mm/s, the minimal through-pore size dropped to 500 nm. However, this very high resolution comes at the cost of excessively long printing times. The total printing time for a column volume equivalent to that of a typical nano-LC column (75 µm i.d. cylindrical tube with length L=15 cm) has been determined to correspond to 330 and 470 hours for the 50 mm/s and the 10 mm/s scan speed respectively. Other issues remaining to be solved are the need to clad the printed skeleton with a suitable mesoporous layer for chromatographic retention and the need to add a top-wall to the printed channels after the removal of the non-polymerized resin.

1. Introduction

Due to its rapidly expanding possibilities and ever more affordable prices, 3D printing is revolutionizing many scientific and technological fields, ranging from robotics to tissue engineering and from aerospace and automotive industries to biotechnology, and is even at the verge of transforming entire industries [1-7].

In the area of analytical chemistry, a strong boom in reports on the use of 3D printing can be witnessed as well [8,9]. The potential advantages of the ability to manufacture devices with an unlimited freedom of design using 3D printing have given a new impetus to the field of microfluidic-based analytical devices [6,7,10-12]. Devices containing integrated valves [13], pumps and mixers [14-16], and integrated three-dimensional filters capable of separating between the nanoscale and microscale [17] have been printed and tested successfully. Printed micro- and millifluidic platforms have been used for many applications, such as microchip electrophoresis of pre-term birth markers [18], solid-phase extraction and on-chip fluorescent labeling of preterm birth risk biomarkers [19], chemiluminescence detection of contaminants in urine and coffee extracts [20], liquid phase microextraction [21] and online magnetic

nanoparticle sorptive extraction as a front end to liquid chromatography (LC) [22], monolithic pepsin microreactor for UPLC-MS peptide mapping [23], one-step printed monolithic ion exchange adsorbers [24] and multiple others. Furthermore, the use of additive manufacturing for on-line sample handling and analyte separations has been studied [25,26].

With its separation efficiency depending very strongly on the degree of order of the column packing material [27], liquid chromatography is clearly one of the areas in analytical chemistry that could benefit most of the possibilities of 3D printing, conceptually offering a road to produce perfectly ordered flow-through structures with optimized shapes and sizes. Current estimates are that about ½ of the separation efficiency in HPLC is lost to packing heterogeneities such as the inherent random packing of particles and the inevitable occurrence of trans-column packing density gradients [28,29]; problems that would be absent if the packing could be 3D printed. However, 3D printing has in the area of liquid chromatography thus far mainly been used to print ancillary devices (paper-based cassette for paper spray mass spectrometry and for 2D paper chromatography and paper spray mass spectrometry [30]), exterior column housing for both liquid chromatography [31-33] and gas chromatography [34,35], or plates for planar chromatography (microstructured surfaces [36] or thin silica gel layers [37]).

Very few literature reports are published on 3D printing of the chromatographic supports themselves. The first work on 3D-printed chromatographic supports dates back to 2014, showing the ability to manufacture porous media with well-defined packing morphologies. Octahedral beads with an apothem around 115 µm were printed in a simple cubic arrangement [38]. The required flow distributors and flow connectors were printed in the same operation. In follow-up research, different particle shapes were studied in a simple cubic arrangement showing that tetrahedral particles (minimal reduced plate height h_{min}=1.56) are superior to other printed particles geometries, including spheres (h_{min}=1.62). For spherical particles, three packing morphologies were compared, confirming that the face centered cubic arrangement is superior (FCC, h_{min}=1.12) to the body centered cubic (BCC, h_{min}=1.53) and the simple cubic (SC, h_{min}=1.62) arrangement [39], in agreement with computational fluid dynamics research [40]. All particles were manufactured having an equivalent particle diameter around 580 µm, and a column porosity of 0.37. 3D printing has also been proposed for the fabrication of a cellulose chromatographic column for the purification of viral particles [41]. This column was filled with a 3D-printed packing designed according to the Schoen-Gyroid geometry, having channel sizes of 300 µm in diameter and a column porosity of 0.5. Very recently, large-volume columns with simple cubic grid morphologies having a minimal feature size of 20 µm have been printed using hybrid stereolithography (HSLA). Minimal reduced plate height of 2.25 have been demonstrated [42].

The spatial resolution and feature size that are required in analytical scale chromatography (HPLC), on which the present study is focused, is at least one order of magnitude smaller than obtained in the aforementioned studies. With particle sizes in commercial columns down to the 1.5 to 2 µm-range and considering that the average interstitial pore sizes in a random sphere packing are about one third of the particle size, it can be argued that a 3D-printed chromatographic support would need through-pores in the order of 1 µm or less to be competitive in the arena of analytical scale chromatography (one third of 1.5 µm is 0.5 µm, but the advantage of the order allows to gain a factor of two, hence the $\leq$1 µm target through-pore size).

One of the most affordable, easy to use and most versatile 3D printing approaches, i.e., filament deposition, has feature sizes on the order of 200 µm at the very best. Optical techniques on the other

hand are inevitably limited to photocurable resins but offer superior resolutions. The best digital light processing (DLP) printer can print features on the order of 50 µm, while inkjet/polyjet (i3DP) printers have a resolution limit of 20 µm. As the required pixel size to produce chromatography packings that are competitive in HPLC applications is smaller than the wavelength of visible light, these techniques are not suited either. The only approach capable of achieving the required $\leq$1 µm resolution is Two-Photon Polymerization (2PP) [43], requiring the absorption of two instead of only one photon to activate the photo-initiator molecules. Consequently, only the very inner core of the focal spot has a high enough photon density to achieve a significant degree of polymerization. The 2PP technology has first been developed by Maruo in 1997 [44] and was first commercialized in 2007 [45].

In the present study, we explore the possibility to use 2PP printing to produce support structures with micrometer-sized through-pores for use in analytical scale chromatography. For this purpose, we made a detailed study of the effect of the main exposure parameters (scan speed and average laser power) that can be tuned to find the best trade-off between print quality and print speed. Two different support types were studied: cylindrical pillar arrays (2.5D) and a monolithic scaffold structure (true 3D). The former has been considered to compare 3D printing with another manufacturing method for miniaturized chromatography systems that has gained increasing interest in the past years, i.e., silicon micromachining [46-48].

2. Experimental methods

All experiments were conducted with a Nanoscribe Photonic Professional GT+ printer [website Nanoscribe] using the built-in galvano scanner to scan the laser beam within the field of view of a high-magnification (63x) large-numerical aperture (NA=1.4) microscope objective to locally initiate radical polymerization inside a droplet of negative photoresist. The commercial IP-DIP photoresist (Nanoscribe GmbH, Eggenstein-Leopoldshafen/BW, Germany), optimized by Nanoscribe GmbH for high resolution printing (minimal XY feature size of around 200 nm), was used in the dip-in configuration (i.e., objective immersed in the liquid). All structures were manufactured on fused silica (FS) glass substrates, which were pretreated with 3-(Trimethoxysilyl)propyl methacrylate (Sigma Aldrich, Diegem, Belgium) to increase adhesion of the printed structures.

The printing process can be divided into three steps. First, all geometries were designed using Solidworks (Dassault Systèmes Solidworks, Waltham, MA, USA), from where they were exported as Standard Tessellation Language (STL) files. Secondly, these files were processed using Nanoscribe's own printing job preparation software, Describe. The following parameters were set: a slicing distance of 200 nm, a hatching distance of 150 nm in the solid fill mode, and the galvo scan mode with a constant exposure in the Dip-in Laser Lithography (DiLL) configuration. Although having a lower printing accuracy, galvo scan mode was chosen above piezo scan mode because of its higher printing speeds [49]. Piezo settling time, galvo acceleration, and stage velocity were kept at their default value given by the Describe software. Laser power and scan speed were the two main exposure parameters modified during these experiments. LP is expressed throughout this article as a percentile, with 100% corresponding to 50mW [Nanoscribe, website]. Finally, all information is sent to the Photonic Professional GT+ printer to fabricate the desired geometries.

After the printing process was finished, uncured photoresist material was removed via dissolution by washing the prints for 20 minutes in propylene glycol monomethyl ether acetate (PGMEA) (Sigma

Aldrich, Diegem, Belgium), after which the samples were rinsed during two minutes in isopropyl alcohol (IPA) (Chem-Lab, Zedelgem, Belgium). No baking step was required.

All printed structures were analyzed using a scanning electron microscope (SEM) (Jeol iT300, Zaventem, Belgium) and a field emission scanning electron microscope (FE-SEM) (Jeol JSM-7100F). Read-out accuracy was on the order of 10-20 nm for pictures taken within the x,y-plane. Samples were gold coated via sputtering with a 4 nm thick layer to avoid or minimize charging effects and to protect the polymer material against the electron beam. The printing quality of the pillars was automatically measured using image processing in Matlab (The MathWorks, Natick, MA, USA) and the dimensions of the Tetrahedral Skeleton Monolith (TSM) were manually measured using ImageJ (NIH, Bethesda, MD, USA).

3. Results and discussion

3.1 Micro-pillar arrays (2.5D structures)

Our initial experiments focused on the simplest geometry, i.e., the micro-pillar array (2.5D structure). Cylindrical pillar arrays were printed with the same diameter (5 µm) and interpillar distance (1.15 µm) as found in literature (external porosity ε=0.4) [50-53]. All pillars were formed by first printing their contour (using the "Contour" function), followed by linearly filling up the central part of each pillar. The study started with a full factorial design exploration of the effect of laser power (LP) and scan speed (SS) on the printing quality on fused silica substrates (pillar height=3 µm). The LP was varied in steps of 10% between 10 and 100%. The SS was varied in steps of 10 mm/s between 10 and 100 mm/s. A set of representative SEM pictures is shown in Fig. 1.

Fig. 2a subsequently shows the resulting pillar diameters as measured by SEM image analysis. The error bars represent the standard deviation on 20 pillars taken from the same array, and as such represent the "within structure" variability. For the envisioned chromatography application, where bed uniformity is of utmost importance, this variability is more practically relevant than the variability between different prints (see Fig. S-1 in the SI, showing that the magnitude of the day-to-day variations is on the order of 100nm).

As can be noted, not all tested LP and SS combinations are represented in Fig. 2a. The conditions that were left out are the ones leading to unsatisfactory printing results. When the LP is too low and/or the SS is too high, the pillars are under-polymerized (see for example at LP=50% and SS=70 mm/s in Fig. 1b). Structures were even completely absent for all conditions with LP$\leq$30%. The higher the SS, the higher the LP that is needed to reach the 2PP threshold and prevent under-polymerization, as can be witnessed from the fact that the number of missing data points towards the high SS end of the curves in Fig. 2a increases with decreasing LP. The LP should however also not be too high. None of the explored LP=100%-conditions is represented in Fig. 2a as the corresponding printed structures all displayed clear signs of over-exposure, leading to the formation of micro-bubbles deforming the printed structures (see example in Fig. 1c). In agreement with one's physical expectations, this type of damage is more pronounced with increasing exposure time (i.e., with decreasing SS), as can be witnessed from the fact that the data points in the low SS-range of the LP=90%-line are missing as well.

The link between the LP and the degree of polymerization, which in turn co-determines the voxel size, is also clearly reflected in the consistent downward shift (from high LP to low LP) of the constant LP-curves in Fig. 2a. At the highest LP, the printed pillars have a diameter of about 5.45 µm, i.e., 0.45 µm larger

than designed in the CAD drawing. The occurrence of such an excess size, further referred to as the "halo"-effect, was systematically observed in the present study and is probably due to a combination of effects: an accumulated dose due to the proximity effect [54-56], as well as the fact that the printing software "fires" a voxel as soon as the center point of the laser beam reaches the printing region indicated on the CAD drawing. Consequently, half of the printed voxel is situated outside the printing region indicated in the CAD file. As can clearly be observed from Fig 2a, the halo-effect increases with increases LP, in agreement with physical expectations. Another observation is that the printed diameter slightly decreases with increasing scan speed for all LP≤80%-cases. This is in obvious agreement with the fact that, the higher the scan speed, the shorter the exposure time, the lower the concentration of radicals, and hence the smaller the voxel size and its concomitant halo-effect. The lower the LP, the more pronounced this scan speed effect becomes (cf. the steepening of the constant LP-curves in Fig. 2a with decreasing LP). Another noteworthy point is that the resulting pillar diameters are smaller than designed in the CAD-file for all LP≤40%. This is most likely because the received dose of light is in this case so weak that only the central parts of the voxel, where the photon density is highest, receives enough energy to induce polymerization.

The presence of the "halo"-effect also influences the inter pillar distance, and thus also the external porosity of the packed bed (see Fig. S-2 in SI). Furthermore, it implies that, in order to print pillars with a diameter exactly matching the target value, the drawing on the CAD file needs to be adjusted to compensate for this halo-effect. Given the expected dependency of the halo-size on both the SS and LP, this is most conveniently done via a calibration run involving a series of different pillar sizes printed at a chosen optimal SS and LP combination to establish the relation between the pillar CAD-diameter ($d_{p,CAD}$) and the finally printed pillar diameter ($d_{p,SEM}$) such that the CAD-diameter providing the exact halo-effect compensation can be determined via interpolation (see Fig. S-3 in SI for example). Moreover, given the relatively poor day-to-day reproducibility (order of 100 nm) that was observed with the instrument (see Fig. S-1 in SI), this calibration should best be repeated on a daily basis for the highest accuracy.

While all data points in Fig. 2a represent conditions producing pillars with the desired global circular circumference, it should be noted that, when looking in detail at this circumference, the pillars obtained at the highest scan speeds displayed some clear local undulations. In the most severe cases (LP=70% at SS=100 mm/s; LP=80% at SS ≥ 90 mm/s, and LP=90% at SS ≥ 80 mm/s), these undulations grow into unidirectional streaks that can even cover the entire inter-pillar gap (see Fig. 1g for example). As the direction of these streaks coincides with the direction of the laser movement, their presence can be clearly attributed to the fact that under these conditions the laser beam moves too fast to keep the polymerization confined to the intended location.

Overall, it was found that SS=50 mm/s and LP=70% provided the best compromise between writing speed and absence of deformations. These conditions were subsequently maintained in an experiment wherein pillars with ever smaller diameters were printed to explore the lower printing size limit (Fig. 2b). As can be noted, the ratio between the actual pillar size as measured by SEM and the nominal pillar size ($d_{p,SEM}/d_{p,CAD}$) is everywhere larger than unity, indicating oversize printing. The ratio also clearly increases with decreasing $d_{p,CAD}$, indicating the problem becomes relatively more important when trying to print smaller features, in full agreement with physical expectations. To investigate this in a more quantitative way, the dashed data curve has been added. This curve has been obtained by recalculating the ratio after including the 400 nm excess diameter that can be expected from the aforementioned "halo"-effect in the value for $d_{p,CAD}$ (corrected ratio= $d_{p,SEM}/(d_{p,CAD}+400\ nm)$). The fact that this recalculated ratio

assumes a value close to unity over a broad range of $d_{p,CAD}$-values ($d_{p,CAD} \geq 1$ µm) shows that the excess diameter observed over this range can indeed be ascribed to the 400 nm halo-effect. For $d_{p,CAD} \leq 1$ µm, i.e., when approaching the technology's resolution limit, an extra deviation appears to be superposed on the 400 nm halo-effect, as its addition to $d_{p,CAD}$ is clearly no longer sufficient to explain the excess diameter. Our current hypothesis for this extra oversize printing effect is the following. Pillars were printed using the Contour-function, wherein the laser follows a circular trajectory along the pillar circumference to maximize its cylindrical shape. However, the galvano scanners used to steer the laser trajectory have difficulties to accelerate and decelerate on this small scale and at the used high printing speeds, resulting in larger printed diameters and deviations from the ideal cylindrical shape. Furthermore, pushing the printer to its performance boundaries might also lead to higher local photon density differences, potentially leading to additional deviations.

At the smallest $d_{p,CAD}$, the $d_{p,SEM}/d_{p,CAD}$-curve tends to form a vertical asymptote. This asymptote corresponds to an actual pillar diameter of $d_{p,SEM}$=950 nm, which can thus be put forward as the lower pillar printing limit for this set of printing conditions. As can be noted from Fig. 1d, the pillars obtained at these dimensions no longer have the desired cylindrical shape. Most probably because of the limited number of voxels that can be fitted on sub-micrometer diameters (pixilation effect) combined with the aforementioned galvano scanner inertia issues. Shifting to lower printing speeds, this can be improved (cf. Fig. 1h where SS=10 mm/s), but this improvement inevitably comes at the expense of a larger printing time. For the sake of completeness, it should be mentioned that 2PP is capable of printing features with significantly smaller dimensions than the ones shown here [57]. However, these pillars are less homogeneously distributed and show a poor shape uniformity.

When 3D printing a chromatography column, an important question is also how large the column's cross-section can be made, because this determines the achievable flow rate. As the width of the column is limited by flow distribution issues as well as by the available substrate surface, the channel depth (or equivalently, the pillar height) becomes the key factor determining the cross-sectional flow-through area. The pillar height and pillar height aspect ratio (ARs) that can be maximally achieved with 2PP has therefore been investigated. This maximal pillar height turns out to be rather low, as intolerable degrees of pillar bending were observed as soon as the pillar height exceeded 15 to 20 µm (AR of only 3 to 4), as can be noted from Fig. 1e. Such ARs are very small compared to those achievable with silicon micromachining and deep reactive Bosch etching, where ARs of the order of 50 have been reported for pillar diameters as small as 1 µm [58,59]. The pillar bending [60] is however not directly caused by mechanical strength of the pillars but is primarily brought about by their close packing. This assertion is corroborated by the fact that much higher ARs are clearly possible (see Fig. 1f for AR=10-example) when printing pillars in a much more spacious pattern (corresponding to an external porosity near ε=1). According to literature, the pillar bending is caused by capillary forces as a result of the surface tension of the development solvent during its drying process [61-63].

3.2 Tetrahedral Skeleton Monoliths (TSM, 3D structures)

Given the clear limitation to achieve satisfactory pillar heights in pillar array beds (2.5D) with a sufficiently dense packing, it can be expected that true 3D structures would suffer much less from the impeding pillar bending problem observed in Fig. 1e because the height of the individual elements in a regularly connected 3D structure can be limited to a few µm, independently of the desired bed height. For the sake of simplicity, the 3D geometry we considered in the present study is the so-called

tetrahedral skeleton monolith (TSM). This geometry mimics the crystal lattice structure of diamond, where each carbon atom is tetrahedrally bonded to its four neighbors. An important advantage of this TSM structure is that all its structural properties such as external porosity, specific skeleton surface and flow-through pore size, can be calculated using only two parameters: the skeleton unit length (l_s) and the skeleton diameter (d_s) (see Figs. 3a&3e). By varying l_s and d_s, TSM structures with external porosities ranging from $\varepsilon \approx 0$ (percolation threshold) all the way up to $\varepsilon \approx 1$ can be obtained (See Fig. S-4 of the SI). The TSM also displays a high degree of isotropy while still offering a few perfect look-through angles (see Figs. 3b&3f). It also is a structure whose chromatographic properties have already been well-characterized by our group [64-68]. Please note that, next to the TSM, a variety of other 3D structures are conceivable as suitable chromatography supports [69].

A number of the 2PP-printed structures are shown in Figs. 3b-d (ε=80%) and 3f-h (ε=60%), resp. showing four satisfactory prints (Figs. 3b-c&3f-g), one over-exposure example (Fig. 3d) and one under-polymerization example (Fig. 3h). Making a full factorial design exploration of the effect of LP and SS, the data set in Fig. 4a is obtained. As can be noted, the number of data points appearing in the plot is different from that in the 2.5D pillar case (cf. Fig. 2a), despite the applied conditions were identical. It furthermore also differs between the ε=80% and the ε=60% TSM. As the data points retained in the plot represent the conditions not suffering from either over-exposure or under-polymerization, the different number of data points implies the selection of the optimal printing parameters ideally needs to be repeated whenever a new geometry is considered. Compared to the 2.5D pillar array considered in Fig. 2a, the working range observed for the 3D structures is considerably narrower. This is undoubtedly linked to the smaller feature size we considered in the latter case (1.5 µm for the TSM vs. 5 µm for the pillar array). Another factor determining the size of the usable printing parameter space certainly is the density of the printed structure, for the number of high scan speed conditions suffering from severe under-polymerization is clearly larger when printing the denser ε=60% TSM compared to the ε=80% TSM.

The rest of the trends is very similar to what was already observed in Fig. 2 for the 2.5D-case. The $d_{s,SEM}/d_{s,CAD}$ -ratio (Fig. 4b; primary y-axis) follows a similar relation as observed in the pillar case, with the $d_{s,SEM}/d_{s,CAD}$-ratio lying clearly above unity, indicating oversize printing and clearly increasing with decreasing feature size. Again accounting for a presumed 400 nm halo-effect by calculating a modified ratio ($d_{s,SEM}/(d_{s,CAD}$+400 nm)), we see the modified ratio (dashed curves) nicely turns to unity for large $d_{s,CAD}$, confirming the occurrence of a 400 nm halo-effect similar to the pillar array case. However, whereas the modified ratio remained basically constant around unity in the pillar array case, the modified ratio now only equals unity for the largest skeleton size and steadily departs from unity with decreasing $d_{s,CAD}$. It can be assumed this is due to the 3D shape of the skeleton and the through-pores, inevitably leading to an extra accumulation of excess voxels compared to the simple cylindrical pillar case, where the printing is a pure 2D process.

The utmost left data points ($d_{s,CAD}$=650 nm in the 80% TSM-case; $d_{s,CAD}$=900 nm in the 60% TSM-case) are considered as the minimal printable size for the LP=70% and SS=50 mm/s parameter set. Below this size, through-pores are starting to be completely solidified due to the halo-effect (see Fig. S-12a&12c as an example). These minimal printable diameters corresponded to real printed skeleton diameters being $d_{s,SEM}$=1.30 µm (80% TSM) and $d_{s,SEM}$=1.70 µm (60% TSM), respectively. Corresponding through-pore sizes (determined as 2*apothem read-out from the SEM) respectively are 870 nm and 510 nm.

Given the importance of the external porosity in liquid chromatography [7], Fig. 4b also provides an estimate of the actual external porosity (cf. the secondary y-axis). This estimate is based on the measured value of the skeleton thickness and edge length and the fixed relation between both parameters and the porosity that exists in a TSM structure (see Fig. S-5 of the SI).

As can be noted from the blue and green curves in Fig. 4b, all printed structures produce a porosity lying well below the target porosity value, respectively lying at 80 and 60%. In addition, it is also obvious that, the smaller the desired feature size, the smaller the actual porosity becomes. For the smallest prints, this decrease in obtained porosities eventually leads to external porosities as small as ε=30% (80%TSM) and even ε=10% (60%TSM). All these observations again point at the occurrence of oversize printing, again also implying that, in order to produce a print displaying the desired porosity, the halo-effect should be anticipated for in the CAD-drawing. This is further confirmed by the dashed line curves in Fig. S-6, showing that if the expected porosity would be calculated for a skeleton that is 400 nm thinner than the actual measured skeleton size (to remove the halo-effect), this porosity would lie much closer to the 80% and 60%-target values. This holds especially for the largest skeleton sizes and the 80% porosity case.

Other important geometric parameters are the external surface of the printed structure and the volume of the through-pores. In a 2D-cut, these correspond to the perimeter P and the area A of the through-pores, respectively. Their values, as well as their ratio are represented in Fig. S-7 of the SI, while the relative variation (=pore-to-pore variation within same printed structure) on this ratio ($\sigma_{A/P}$) is given in Fig. 5a. A duplicate print for the utmost left data points ($d_{s,CAD}$=650 nm in the 80% TSM-case; $d_{s,CAD}$=900 nm in the 60% TSM-case) was analyzed to check the effect of print-to-print variability on $\sigma_{A/P}$, showing only 2% of variation for both 60% and 80% case. The pore-to-pore variation of the A/P-ratio can be expected to play an important role in the band broadening process in a chromatographic experiment, as it can be expected to directly translate into a pore-to-pore variation in velocity, which in turn can give rise to the short-range eddy-dispersion described by Giddings [70]). The relation between the A/P-ratio and the local velocity can be inferred from Kozeny-Carman's law [71], stating that $u \sim (A/P)^2$. From this relation, it can be assumed the relative velocity difference between neighboring through-pores will be given by:

$$\frac{\Delta u}{\bar{u}} = \frac{4\sigma_{A/P}(1+\sigma_{A/P}^2)}{1+6\sigma_{A/P}^2+\sigma_{A/P}^4} \quad (1)$$

This expression can subsequently be inserted directly into Giddings' expression for the mechanic contribution to the eddy-dispersion ($h_{eddy,m}$ representing the upper limit for the eddy-dispersion reached in the high velocity limit):

$$h_{eddy,m} = \frac{1}{4}\left(\frac{\Delta u}{u}\right)^2 \frac{l_{dom}}{d_{dom}} \quad (2)$$

with l_{dom} defined as the axial distance from the center of one through-pore up to the center of a neighboring through-pore, and d_{dom} equal to the sum of the skeleton diameter and the apothem of a hexagonal through-pore.

The resulting $h_{eddy,m}$-values are shown in Fig. 5b as a function of the desired feature size. While the estimated $h_{eddy,m}$-contribution can be considered negligible in the 80%-TSM case, it becomes really significant in the 60%-TSM case for structures with a skeleton size below 1 μm, where $h_{eddy,m}$=0.1 to 0.3. Compared to a perfect TSM, for which a band broadening around h=0.8-1 that can be expected, this

extra eddy-dispersion contribution is indeed significant. [8,9] Again, a duplicate print for the utmost left data points was analyzed to check the effect of print-to-print variability on $h_{eddy,m}$, showing only 4% and 7% of variation for the 60% and 80% case, respectively.

Next to clear size deviations, printing structures near the resolution limit of the system also leads to clear shape deviations, as the through-pores (perfect regular hexagons in the CAD-drawing) become increasingly circular when the lower printing limit is approached. Trying to quantify this phenomenon, several geometrical measures were considered. The measure based on the "hexagonicity" was plagued by the presence of local undulations on the perimeter (see Fig. S-8 in the SI). These undulations considerably increase the perimeter over that of a hexagon with smooth sides, thus skewing the expected area to a value below unity without actually reflecting the global shape of the through-pores.

A more stable parameter to quantify the observed transition between a near-perfect hexagon and the highly circular through-pores observed when moving from the largest to the smallest print sizes was the angle of the corners (see Fig. S-9). Fig. S-9c shows the angle for the 80% TSM indeed consistently increases from 122° (which is close to the 120° of a perfect hexagon; deviation only caused by the local roughness of the print) for the largest $d_{s,CAD}$-value to above 130° for the smallest $d_{s,CAD}$-values. For the 60% TSM, the angles are consistently larger than in the 80% TSM-case, eventually reaching values up to 145°. Given the fixed voxel size, the smaller perimeter of the 60% TSM is inevitably made up of fewer voxels, which inevitably leads to more rounded corners. As a moderation, it should be considered that, in view of the chromatography target application, the exact shape of the through-pores is much less critical than for example the pore-to-pore variation of the permeability discussed in Fig. 5a. All other considered possible shape measures all give a similar picture: good compliance at large skeleton size and growing deviation from this shape with decreasing size (see Fig. S-10 for extra example).

Returning to the lower skeleton size limits encountered for the TSM (leftmost data points in Fig. 4b), it should be considered the observed lower limit results from an optimization carried out for the case of a 1.5 µm skeleton. To explore the possibility to further reduce the skeleton size, a new full factorial design was run at the original lowest size limit. Not surprisingly, this optimization shifted printer settings into the direction of a lower SS, where the movements of the galvano scanner can be better controlled. To prevent over-exposure, the decrease in SS obviously was accompanied by a decrease in LP. As can be noted from Fig. 6, the re-iterated optimal conditions lead to clear structural improvements for the lower limit structures (compare Fig. 6b with 6c and Fig. 6e with Fig. 6f) thus lowering the minimal printable through-pore size (=2*apothem) from 1.05 µm (corresponding to 39% porosity) to 530 nm (corresponding to 30% porosity) for the 80% TSM and from 530 nm to 400 nm for the 60% TSM. Below this minimal size, some through-pores are partially closed (see Fig. S-12a-2&b-2&c-2&d-2 of the SI) or the print displays an extreme degree of heterogeneity (Fig. S-11c).

Obviously, the higher printing quality achieved in Figs. 6c and 6f comes at the expense of a larger printing time. Whereas the results have up till here been interpreted in terms of the scan speed (SS), it should be kept in mind this is a practically less relevant measure than the actual volumetric printing speed, i.e., reflecting the time needed to print a given large volume. The SS-value is merely the set scan speed of the galvo scanner, and it should be realized that this speed cannot be maintained during the entire printing process, given the frequent need to make turns and hence stops. To establish the link between the set scan speed (SS, mm/s) and the true volumetric printing speed (VPS, volume/time), a tetrahedral skeleton monolith column with 80% external porosity and with cross-sectional dimensions

y=215 µm; z=18.75 µm and length 43 µm was printed at different scan speeds (from 10 to 100 mm/s) and the volumetric printing speed (VPS) was calculated from the total time needed to complete the job.

As shown in Fig. S-13, the link between the set scan speed (SS, mm/s) and the actual volumetric printing speed (VPS, volume/time) is highly non-linear and even goes through a clear maximum. This maximum is in fact already achieved around SS=30 mm/s, after which the VPS gradually decreases to the extent that the VPS descends again below the level reached at SS=10 mm/s as soon for all SS≥70 mm/s. Presumably this rather unexpected effect is caused by the different relative contributions of the acceleration and deceleration times at the different SS (cf. the many changes in direction needed to print the complex TSM structure). To avoid mechanical vibrations originating from very high SS, longer settling times are needed as stabilization period for the system. Furthermore, this effect can also be influenced by the trajectory of the laser throughout the print. The relation shown in Fig. S-13 will certainly also depend on the exact geometry and dimensions (both macroscopic and microscopic) of the actually printed design, the employed laser power and might be different for other commercial 2PP printers. Nevertheless, having run the calibration experiment for a structure with micro-scale and macroscale dimensions suitable for nano-scale liquid chromatography (the prime region where applications of 3D-printed analytical scale liquid chromatography can be expected), we deem the correlation to be of a good practical relevance for the currently considered Nanoscribe printer.

From Fig. S-13, it can be read-out that the SS=50 mm/s printing conditions leading to the structures in Fig. 6a,d roughly correspond to a VPS of 553 $\mu m^3/s$, whereas the SS=10 mm/s printing conditions used in Fig. 6b-c and Fig. 6e-f correspond to a VPS of 390 $\mu m^3/s$. To print a typical nano-LC column (cross-sectional area corresponding to a 75 µm inner diameter (i.d.) cylindrical tube and L=15 cm), these VPSs correspond to a total printing time of resp. 330 h (at SS=50 mm/s) and 470 h (at SS=10 mm/s), which is deemed impractically high and not economically viable.

Discussion and conclusions

Two-Photon Polymerization (2PP) is clearly capable of achieving the very high printing resolution needed to produce support structures with a through-pore and support size that is competitive with that of state-of-the-art packed bed columns used in analytical liquid chromatography. However, this comes at the cost of a low printing speed, as illustrated above, showing it would take 330 h to print a typical nano-LC column (cross-sectional area corresponding to a 75 µm i.d. cylindrical tube and L=15 cm) with the desired 1 µm-scale through-pore size. Options for parallel printing are being developed [72], but even a multiplication with a factor of 10 or even 100 would still leave the 3D printing route as slow and costly compared to conventional HPLC column manufacturing.

Another impediment is the option of available materials. 2PP printing is limited to a very restricted group of 2PP-optimized resins, mostly of the acrylic type. 2PP in polymers with proven suitable chromatographic properties, such as polystyrene divinylbenzene or polymetacrylate is still in its infancy [73-75]. The presently printed material furthermore lacks any mesoporosity, such that an additional cladding step with a meso-porous layer via e.g., sol-gel deposition, is mandatory. In a first approach, one could start from an 80% TSM with $d_{s,CAD}$=1.5 µm and clad it with a 250 nm mesoporous shell layer to obtain a 65% TSM [76]. Given the need to flush the structure with a very viscous sol, the cladding process can however be expected to be very cumbersome and prone to column-to-column variations. In addition, it adds a very time-consuming step to the manufacturing process, a step that is absent in conventional column manufacturing.

Next to the cladding issue, there is also the problem of column sealing. As the 2PP resins are very viscous (2420 cP at 20°C), they cannot be removed in a flush-through mode and hence have to be removed while the print is still open and hence fully accessible to the development solvents. This implies the top-wall of the structure cannot be added via 2PP printing but needs to be added afterwards. Solutions involving adhesive glue bonding, dry film photoresist bonding, or clamping can be conceived, but these are prone to leaks, clogged channels, and the formation of preferential flow paths between the printed structure and the top plate.

Along with the chemical nature of the printed material also comes the issue of its mechanical strength. The IP-DIP material used in the present study for example has a Young's modulus of only 3 GPa, which is one order of magnitude smaller than that of silica and nearly two orders of magnitude smaller than (factor 50 to be precise) than that of silicon. It is therefore still uncertain whether these 2PP printed structures will withstand the high pressures and shear rates prevailing in an HPLC column.

Not only is the 2PP technology limited in the choice of resin material, it is also limited in the choice of the channel substrate. Silicon is often used in microsystem technologies due to its interesting properties and easy to use nature. For 2PP applications, however, photons are strongly reflected by the silicon's surface, resulting in a less controllable photon distribution and a corresponding smaller zone of good main exposure printing parameters (LP and SS). Other substrates such as PDMS and other thermoplastics (PMMA, COC,…) can be less well suited either due to the observed local melting issues when focusing the laser beam onto the substrate's surface, and furthermore, a minimum refractive index contrast between substate and photoresist is required for automatically finding the interface on which substrates are manufactured, a condition considerably constraining the substrate material choice. Alternative approaches (e.g., the use of the auto-fluorescence signal of the photoresist) are currently being used to enhance the interface detection. Further improvements of the resolution can be expected by improving the liquid resin composition, as was very recently done with the introduction of IP-DIP2.

In addition, the 2PP printing technology is not flawless, as was demonstrated in the present study. When approaching the lower through-pore size limit ($d_{s,CAD} \leq 1$ µm), a significant degree of structural heterogeneity develops. In case of the ε=60% TSM, this can lead to a significant eddy-dispersion contribution (extra h-contribution on the order of 0.1-0.3 reduced h-units compared to the h=0.8-1-level that is expected for a flawless TSM structure).

Yet another problem is the relatively poor day-to-day repeatability of the prints, at least in our hands (order of 100 nm variability; see Fig. S-13 in the SI).

Overall, it seems the number of hurdles to overcome to produce competitive 2PP chromatography columns are still quite significant and it is at present therefore still unclear whether 2PP printing will be able to replace the conventional column packing methods using spherical particles in the near future. Nevertheless, if printing speed could be boosted and the choice of materials could be extended, the printing resolution and the freedom of structural design offered by the 2PP are truly unique assets to continue evaluating this technology as a promising road to produce the perfect chromatographic packing material.

References

[1] Schmitt, F.; Piccin, O.; Barbé, L. ; Bayle, B. *Front. Robot. AI* **2015**, 5, 84.

[2] Palenzuela, C. L. M. ; Pumera, M. *TrAC* **2018**, 103, 110-118.

[3] Murphy, S. V. ; Atala, A. *Nat. Biotechnol.* **2014**, 32 (8), 773-785.

[4] Uriondo, A. ; Esperon-Miguez, M. ; Perinpanayagam, S. *Proc Inst Mech Eng G J Aerosp Eng* **2015**, 229 (11), 1-16.

[5] Delić, M. ; Knežević, B. ; Škrobot, P. J. *Bus. Logist.* **2017**, 17, 421-436.

[6] Gross, B. C. ; Erkal, J. L. ; Lockwood, S. Y. ; Chen, C. ; Spence, D. M. *Anal. Chem.* **2014**, 86, 3240-3253.

[7] Ho, C. M. B.; Ng, S. H.; Li, K. H. H.; Yoon, Y. J. *Lab Chip* **2015**, 15, 3627−3637.

[8] Kalsoom, U. ; Nesterenko, P. N. ; Paull, B. *TrAC* **2018**, 105, 492-502.

[9] Nesterenko, P. N. *Pure Appl. Chem.* **2020**,92 (8), 1341-1355.

[10] Nielsen, A. V. ; Beauchamp, M. J. ; Nordin, G. P. ; Woolley, A. T. *Annu Rev Anal Chem* **2020**, 13, 1.1-1.21.

[11] Tetala, K. K. R. ; Vijayalakshmi, M. A. *Anal. Chim. Acta* **2016**, 906, 7-21.

[12] Balakrishnan, H. K. ; Badar, F. ; Doeven, E. H. ; Novak, J. I. ; Merenda, A. ; Dumée, L.F. ; Loy, J. ; Guijt, R. M. *Anal. Chem.* **2021**, 93, 350-366.

[13] Rogers, C. I.; Qaderi, K.; Woolley, A. T.; Nordin, G. P. *Biomicrofluidics* **2015**, 9(1), 016501.

[14] Maruo, S. ; Inoue, H. *Appl. Phys. Lett.* **2006**, 89, 144101.

[15] Gong, H. ; Woolley, A. T. ; Nordin, G. P. *Lab Chip* **2016**, 16, 2450-2458.

[16] Gong, H. ; Woolley, A. T. ; Nordin, G. P. *Biomicrofluidics* **2019**, 13 (1), 014106.

[17] Amato, L. ; Gu, Y. ; Bellini, N. ; Eaton, S. M. ; Cerullo, G. ; Osellame, R. *Lab Chip* **2012**, 12, 1135.

[18] Beauchamp, M. J. ; Nielsen, A. V. ; Gong, H. ; Nordin, G. P. Woolley, A. T. *Anal. Chem.* **2019**, 91(11), 7418-7425.

[19] Bickham, A. V. ;Pang, C. ; George, B. Q. ; Topham, D. J. ; Nielsen, J. B. ; Nordin, G. P. Woolley, A. T. *Anal. Chem.* **2020**, 92, 12322-12329.

[20] Gupta, V. ; Mahbub, P. ; Nesterenko, P. N. ; Paull, B. *Anal. Chim. Acta* **2018**, 1005, 81-92.

[21] Worawit, C. ; Cocovi-Solberg, D. J. ; Varanusupakul, P. ; Miró, M. *Talanta* **2018**, 185, 611-619.

[22] Wang, H. ; Cocovi-Solberg, D. J. ; Hu, B. ; Miró, M. *Anal. Chem.* **2017**, 89, 12541-12549.

[23] Jönsson, A. ; Svejdal, R. R. ; Bøgelund, N. Nguyen, T. T. T. N. ; Flindt, H. ; Kutter, J. P. ; Rand, K. D. ; Lafleur, J. P. *Anal. Chem.* **2017**, 89, 4573-4580.

[24] Simon, U. ; Dimartino, S. *J. Chrom. A.* **2019**, 1587, 119-128.

[25] Cocvi-Solberg, D. J. ; Worsfold, P. J. ; Miró, M. *TrAC* **2018**, 108, 13-22.

[26] Li, F. ; Ceballos, M. R. ; Balavandy, S. K. ; Fan, J. ; Khataei, M .M. ; Yamini, Y. ; Maya, F. *J Sep Sci* **2020**, 43, 1854-1866.

[27] Billen, J. ; Gzil, P. ; Desmet, G. *Anal. Chem.* **2006**, 78, 6191-6201.

[28] Matheuse, F. ; Deridder, S. ; Desmet, G. *J. Chrom. A.* **2020**, 1634, 461710.

[29] F. Gritti, M. Farooq Wahab, *LCGC North America* **2018**, 36, 82-98.

[30] Cheng, M.-H. ; Lin, C.-H. *Proc. IEEE Int. Conf. Micro Electro Mech. Syst.* **2018**, 1233-1236.

[31] Sandron, S.; Heery, B.; Gupta, V.; Collins, D. A.; Nesterenko, E. P.; Nesterenko, P. N.; Talebi, M.; Beirne, S.; Thompson, F.; Wallace, G. G.; Brabazon, D.; Regan, F.; Paull, B. *Analyst* **2014**, 139, 6343-6347.

[32] Gupta, V. ; Talebi, M. ; Deverell, J. ; Sandron, S. ; Nesterenko, P. N. ; Heery, B. ; Thompson, F. ; Berine, S. ; Wallace, G. G. ; Paull, B. *Anal. Chim. Acta* **2016**, 910, 84-94.

[33] Gupta, V. ; Beirne, S. ; Nesterenko, P. N. Paull, B. *Anal. Chem.* **2018**, 90(2), 1186-1194.

[34] Lucklum, F. ; Janssen, S. ; Lang, W. ; Vellekoop, M. J. *Procedia Eng.* **2015**, 120, 703-706.

[35] Phyo, S. ; Choi, S. ; Jang, J. ; Choi, S. ; Lee, J. *Lab Chip* **2020**, 20, 3435-3444.

[36] Macdonald, N. ; Currivan, S. A. ; Tedone, L. ; Paull, B. *Anal. Chem.* **2017**, 89 (7), 2457-2463.

[37] Fichou, D. ; Morlock, G. E. *Anal. Chem.* **2017**, 89, 2116-2122.

[38] Fee, C. ; Nawada, S. ; Dimartino, S. *J. Chrom. A.* **2014**, 1333, 18-24.

[39] Nawada, S. ; Dimartino, S. ; Fee, C. *Chem. Eng. Sci.* **2017**, 164, 90-98.

[40] Schure, M. R. ; Maier, R. S. ; Kroll, D. M. ; Davis, H. T. *J. Chrom. A.* **2004**, 1031, 79-86.

[41] Moleirinho, M. G. ; Sean Feast, S. ; Moreira, A. S. ; Silva, R. J. S. ; Alves, P. M. ; Carrondo, M. J. T. ; Huber, T. ; Fee, C. ; Peixoto, C. *Sep. Purif. Technol.* **2021**, 254, 117681.

[42] Nawada, S. ; Budel, T. *LCGC Europe*, **2021**, 381-384.

[43] Serbin, J. ; Ovsianikov, A. ; Chichkov, B. *Opt. Express* **2004**, 12(21), 5221-5228.

[44] Maruo, S. ; Nakamura, O. ; Kawata, S. *Opt. Lett.* **1997**, 22, 132-134.

[45] *Nanoscribe GmbH Home Page*. https://www.nanoscribe.de/en/ (accessed 2021-09-16).

[46] Detobel, F. ; De Bruyne, S. ; Vangelooven, J. ; De Malsche, W. ; Aerts, T. ; Terryn, H. ; Gardeniers, H. ; Eeltink, S. ; Desmet, G. *Anal. Chem.* **2010**, 82, 7208-7217.

[47] Stadlmann, J. ; Hudecz, O. ; Krššáková, G. ; Ctortecka, C. ; Van Raemdonck, G. ; Op De Beeck, J. ; Desmet, G. ; Penninger, J.M. ; Jacobs, P. ; Mechtler, K. *Anal. Chem.* **2019**, 91(22), 14203-14207.

[48] Tóth, G. ; Panić -Janković, T. ; Mitulović, G. *J. Chrom. A.* **2019**, 1603, 426-432.

[49] Zhou, X. ; Hou, Y. ; Lin, J. *AIP Advances*, **2015**, 5, 030701.

[50] Gzil, P. ; Vervoort, N. ; Baron, G. V. ; Desmet, G. *Anal. Chem.* **2003**, 75, 6244-6250.

[51] Vervoort, N. ; Billen, J. ; Gzil, P. ; Baron, G. V. ; Desmet, G. *Anal. Chem.* **2004**, 76, 4501-4507.

[52] Eghbali, H. ; De Malsche, W. ; De Smet, J. ; Billen, J. ; De Pra, M. ; Kok, W. T. ; Schoenmakers, P. J. ; Gardeniers, H. ; Desmet, G. *J. Sep. Sci.* **2007**, 30, 2605-2613.

[53] Eghbali, H. ; Matthijs, S. ; Verdoold, V. ; Gardeniers, H. ; Cornelis, P. ; Desmet, G. *J. Chrom. A.* **2009**, 1216, 8603-8611.

[54] Waller, E. H. ; von Freymann, G. *Polym. J.* **2016**, 8, 297.

[55] Saha, S. K. ; Divin, C. ; Cuadra, J. A. ; Panas, R. M. *J. Micro Nanomanuf.* **2017**, 5, 031002.

[56] Covarrubias, L. P. ; Arnoux, C. ; Carlier, Q. ; Khaldi, A. ; Baldeck, P. ; Heggarty, K. *Proc. SPIE* **2020**, 11349.

[57] Liu, Q. ; Vanmol, K. ; Lycke, S. ; Van Erps, J. ; Vandenabeele, P. ; Thienpont, H. ; Ottevaere, H. RSC Adv. 2020, 10, 14274-14282.

[58] Wu, B. ; Kumar, A. ; Pamarthy, S. *Int. J. Appl. Phys.* **2010**, 108, 051101.

[59] Abdolvand, R. ; Ayazi, F. *Sens. Actuators, A* **2008**, 144, 109-116.

[60] Frommhold, A. ; Robinson, A. P. G. ; Tarte, E. *Microelecton. Eng.* **2012**, 99, 43-49.

[61] Oakdale, J. S. ; Ye, J. Smith, W. L. ; Biener, J. *Opt. Express* **2016**, 24(24), 27077-27086.

[62] Maruo, S. ; Hasegawa, T. ; Yoshimura, N. *Opt. Express* **2009**, 17(23), 20945-20951.

[63] Yang, D.-Y. ; Park, S. H. ; Lim, T. W. ; Kong, H.-J. ; Yi, S. W. ; Yang, H. K. ; Lee, K.-S. *Appl. Phys. Lett.* **2007**, 90, 013113.

[64] Vervoort, N. ; Gzil, P. ; Baron, G. V. ; Desmet, G. *J. Chrom. A.* **2004**, 1030, 177-186.

[65] Gzil, P. ; Vervoort, N. ; Baron, G. V. ; Desmet, G. *J. Sep. Sci.* **2004**, 27, 887-896.

[66] Vervoort, N. ; Saito, H. ; Nakanishi, K. ; Desmet, G. *Anal. Chem.* **2005**, 77, 3986-3992.

[67] Deridder, S. ; Eeltink, D. ; Desmet, G. *J. Sep. Sci.* **2011**, 34, 2038-2046.

[68] Deridder, S. ; Vanmessen, A. ; Nakanishi, K. ; Desmet, G. ; Cabooter, D. *J. Chrom. A.* **2014**, 1351, 46-55.

[69] Salmean, C. ; Dimartino, S. *Chromatographia* **2019**, 82, 443-463.

[70] Giddings, J.C. *Dynamics of chromatography*; New York, M. Dekker, 1965.

[71] Coulson, J. M. ;Richardson, J. F. *Chemical Engineering Volume 2*; Oxford, Butterworth-Heinemann, 1955.

[72] Hahn, V. ; Kiefer, P. ; Frenzel, T. ; Qu, J. ; Blasco, E. ; Berner-Kowollik, C. ; Wegener, M. *Adv. Funct. Mater.* **2020**, 30, 1907795.

[73] Svec, F. ; Lv, Y. *Anal. Chem.* **2015**, 87(1), 250-273.

[74] Walsh, Z. ; Abele, S. ; Lawless, B. ; Heger, D. ; Klan, P. ; Breadmore, M.C. ;Paull, B. ; Macka, M. ; *Chem. Commun.* **2008**, 48, 6504-6506.

[75] Panusa, G. ; Pu, Y. ; Wang, J. ; Moser, C. ; Psaltis, D. *Polymers* **2020**, 12(11), 2485.

[76] Futagami, S. ; Hara, T. ; Ottevaere, H. ; Terryn, H. ; Baron, G. V. ; Desmet, G. ; De Malsche, W. *J. Chrom. A*. **2019**, 1595, 58-65.

Figure captions

Figure 1. SEM pictures of micro-pillar arrays printed under various conditions of laser power (LP) and scan speed (SS)and with variable geometry. **(a)** Perfectly printed pillar array at LP=70% and SS=50 mm/s. **(b)** Pillars showing signs of under-polymerization (printed at LP=50% and SS=70 mm/s). **(c)** Pillars showing signs of over-exposure (printed at LP=90% and SS=10 mm/s). **(d)** Smallest possible pillar diameter ($d_{p,CAD}$=300 nm resulting in $d_{p,SEM}$=950 nm) achieved by printing at LP=70% and SS=50 mm/s. The zoomed in picture clearly shows the loss of the global circular circumference when pushing the printer to its limits. **(e)** A pillar bed having an AR=5 with an external porosity of 50% (printed at LP=90% and SS=50 mm/s). **(f)** A perfectly single standing pillar (external porosity≈1) with AR=10 (printed at LP=90% and SS=50 mm/s). **(g)** Clear local undulations along the laser path due to very high scan speeds. (LP=90% and SS=90 mm/s). **(h)** Zoom-in on pillar with same size as in (d) ($d_{p,SEM}$=900 nm) but now printed at LP=50% and SS=10 mm/s. Target pillar diameter($d_{p,CAD}$) was 5.00 μm in (a-c) and (e-g), and 300 nm in (d,h).

Figure 2. (a) Evolution of the effective pillar diameter measured from SEM pictures ($d_{p,SEM}$) as a function of the applied laser power (LP) and scan speed (SS) of a cylindrical micro-pillar with target diameter ($d_{p,CAD}$) of 5.00 μm. **(b)** Evolution of the ratio the effective pillar diameter ($d_{p,SEM}$) and the target diameter ($d_{p,CAD}$) as a function of $d_{p,CAD}$. The dashed curve represents the ratio that would be expected if the target diameter would have been 400 nm larger ($d_{p,SEM}/(d_{p,CAD}$+400 nm)) to accommodate for the "halo"-effect (see text). Print conditions in (b) are LP=70% and SS=50 mm/s.

Figure 3. (a,d) CAD-Drawings of Tetrahedal Skeleton Model (TSM) rendered under an angle and **(b,f)** showing the porosity of printed TSM structures. **(c,g)** Top-view SEM pictures of same TSM printed under various conditions of laser power (LP) and scan speed (SS). Top row: 80% porosity TSM. Bottom row: 60% porosity TSM. Print parameters: **(b-c,f-g)** LP=50% and SS=10 mm/s ; **(d)** LP=80% and SS=20 mm/s ; **(h)** LP=40% and SS=70 mm/s. Target skeleton diameter($d_{s,CAD}$) was 1.50 μm.

Figure 4. (a) Evolution of the effective pillar diameter measured from SEM pictures ($d_{s,SEM}$) as a function of the applied laser power (LP) and scan speed (SS) for a 80% (black) and 60% (red) TSM with target 1.50 μm. **(b, primary y-axis)** Evolution of the ratio of the effective pillar diameter ($d_{s,SEM}$) and the target diameter ($d_{s,CAD}$) as a function of $d_{s,CAD}$ for the 80% (black) and 60% (red) TSM. The dashed curve represents the ratio that would be expected if the target diameter would have been 400 nm larger ($d_{s,SEM}/(d_{s,CAD}$+400 nm)) to accommodate for the "halo"-effect (see text). **(b, secondary y-axis)** Effective external porosity as measured via Eq. (x1) for the 80% (blue) and 60% (green) TSM. Print conditions in (b): LP=70% and SS=50 mm/s. Error bars represent the in-print pore-to-pore variability.

Figure 5. (a) Evolution of the pore-to-pore standard deviation of the ratio of the through-pores cross-section and perimeter $\sigma_{(A/P)}$ as a function of $d_{s,CAD}$ and **(b)** corresponding predicted short-range eddy-dispersion (see text). Colour code: 80% TSM=black and 60%=red. Print parameters: LP=70% and SS=50 mm/s.

Figure 6. SEM pictures of 80% (top row) and 60% (bottom row) TSM **(a)** $d_{s,CAD}$=650 nm; print conditions: LP=70% and SS=50 mm/s. **(b)** $d_{s,CAD}$=650 nm; print conditions: LP=50% and SS=10 mm/s. **(c)** $d_{s,CAD}$=450 nm; print conditions: LP=50% and SS=10 mm/s. **(d)** $d_{s,CAD}$=900 nm; print conditions: LP=70% and SS=50 mm/s. **(e)** $d_{s,CAD}$=900 nm; print conditions: LP=50% and SS=10 mm/s. **(f)** $d_{s,CAD}$=700 nm; print conditions: LP=50% and SS=10 mm/s.

FIGURE 1

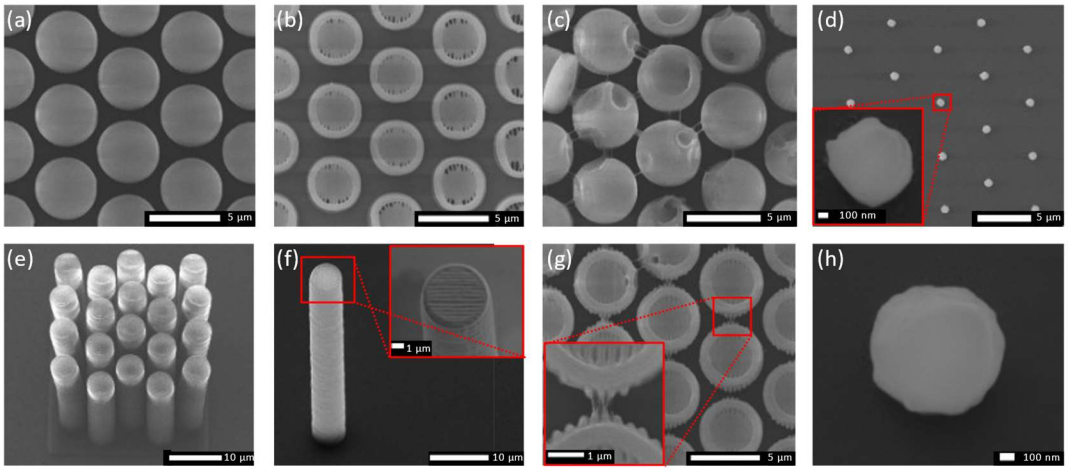

FIGURE 2

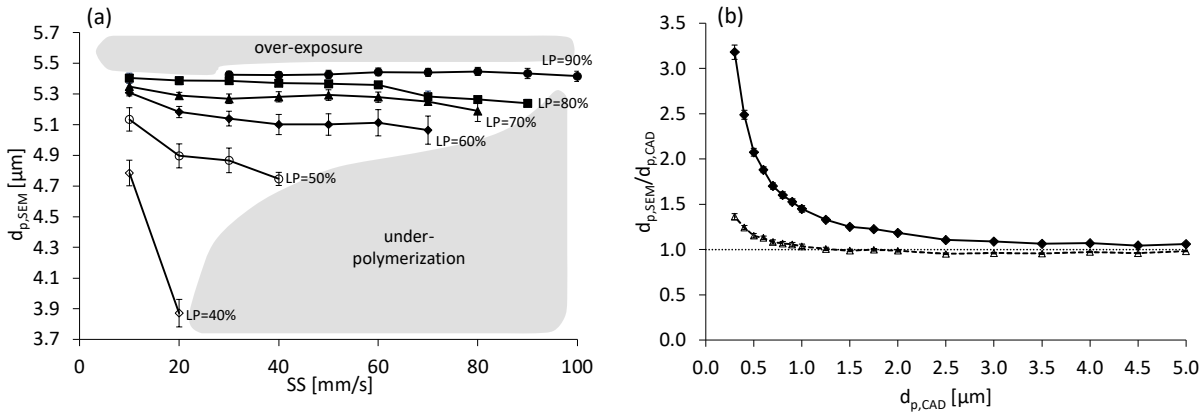
(a)
over-exposure
under-
polymerization
LP=90%
LP=80%
LP=70%
LP=60%
LP=50%
LP=40%
$d_{p,SEM}$ [µm]
SS [mm/s]
(b)
$d_{p,SEM}/d_{p,CAD}$
$d_{p,CAD}$ [µm]

FIGURE 3

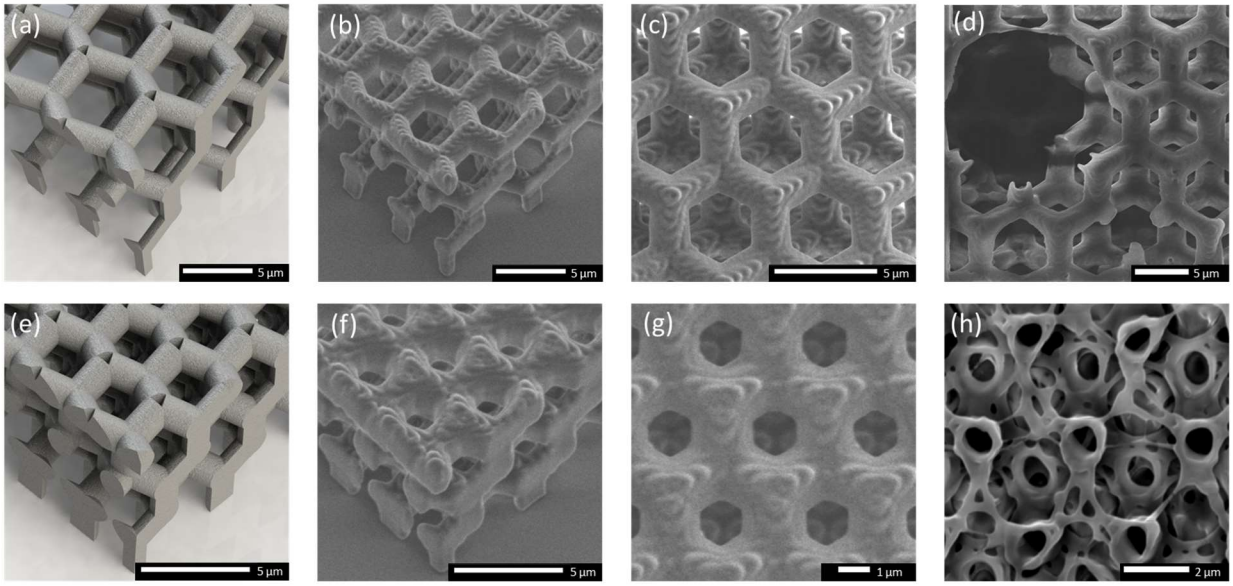

FIGURE 4

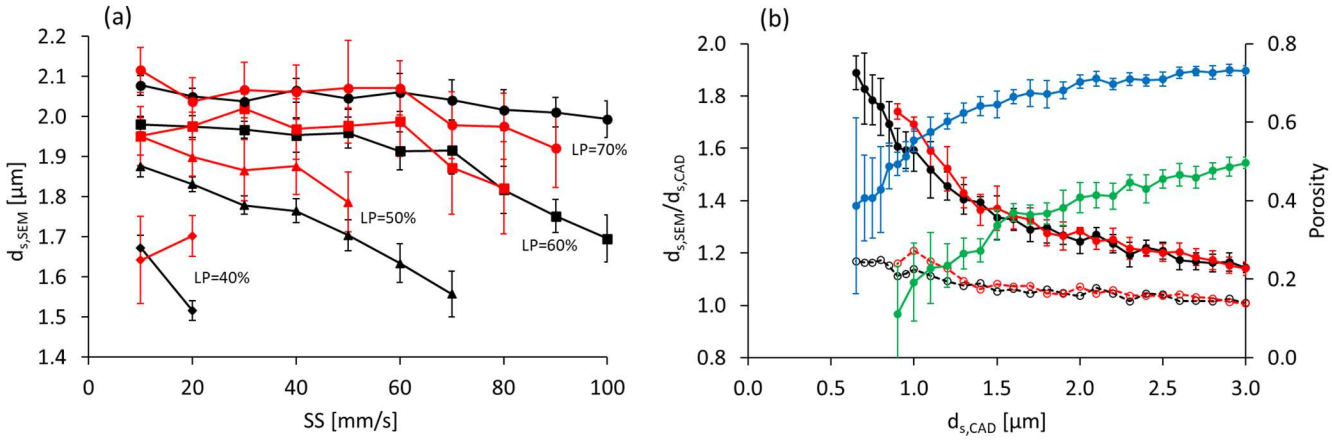
(a)
2.2
2.1
2.0
1.9
1.8
1.7
1.6
1.5
1.4
$d_{s,SEM}$ [µm]
0
20
40
60
80
100
SS [mm/s]
LP=70%
LP=50%
LP=60%
LP=40%
(b)
2.0
1.8
1.6
1.4
1.2
1.0
0.8
$d_{s,SEM}/d_{s,CAD}$
0.0
0.5
1.0
1.5
2.0
2.5
3.0
$d_{s,CAD}$ [µm]
0.8
0.6
0.4
0.2
0.0
Porosity

FIGURE 5

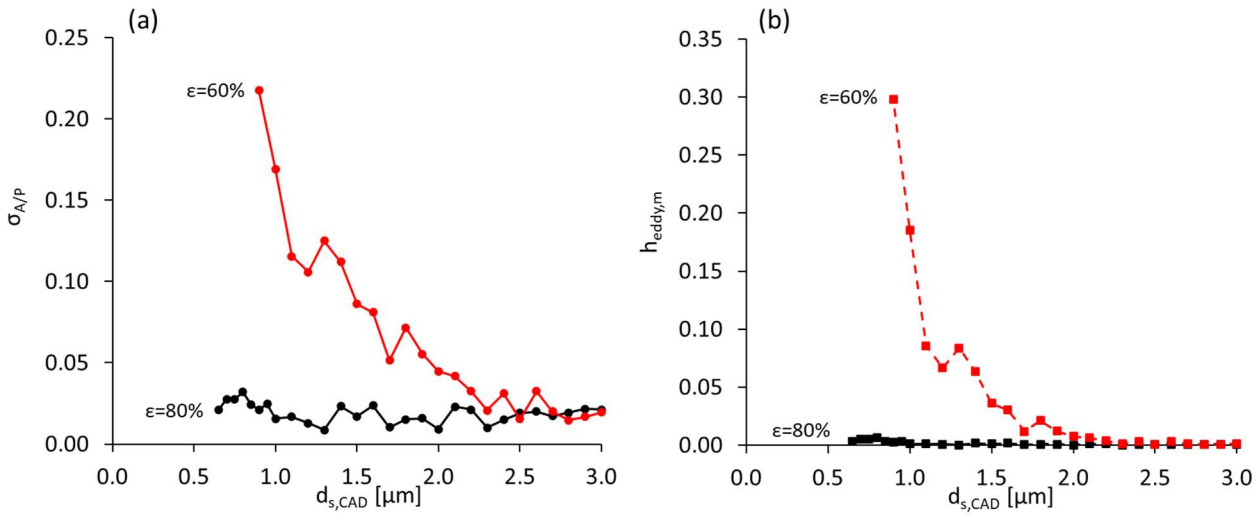
(a)
0.25
0.20
0.15
0.10
0.05
0.00
σA/P
ε=60%
ε=80%
0.0
0.5
1.0
1.5
2.0
2.5
3.0
ds,CAD [µm]
(b)
0.35
0.30
0.25
0.20
0.15
0.10
0.05
0.00
heddy,m
ε=60%
ε=80%
0.0
0.5
1.0
1.5
2.0
2.5
3.0
ds,CAD [µm]

FIGURE 6

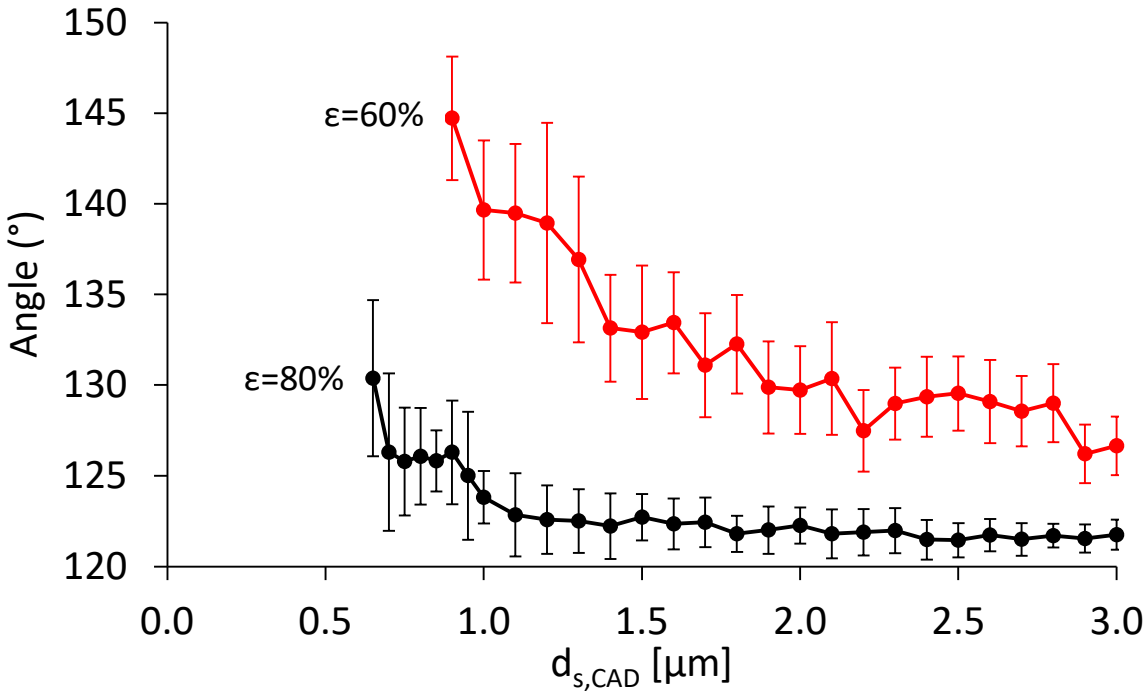
150
145
140
135
130
125
120
Angle (°)
ε=60%
ε=80%
0.0
0.5
1.0
1.5
2.0
2.5
3.0
d s,CAD [µm]

FIGURE 7